

Quantum Visual Feature Encoding Revisited

Xuan-Bac Nguyen^{1*}, Hoang-Quan Nguyen¹, Hugh Churchill²,
Samee U. Khan³, Khoa Luu¹

^{1*}Dept. of Electrical Engineering and Computer Science, University of
Arkansas, Fayetteville, 72703, Arkansas, USA.

²Dept. of Physics, University of Arkansas, Fayetteville, 72703, Arkansas,
USA.

³Dept. of Electrical & Computer Engineering, Mississippi State
University, Starkville, 39762, Mississippi, USA.

*Corresponding author(s). E-mail(s): xnguyen@uark.edu;
Contributing authors: hn016@uark.edu; hchurch@uark.edu;
skhan@ece.msstate.edu; khoaluu@uark.edu;

Abstract

Although quantum machine learning has been introduced for a while, its applications in computer vision are still limited. This paper, therefore, revisits the quantum visual encoding strategies, the initial step in quantum machine learning. Investigating the root cause, we uncover that the existing quantum encoding design fails to ensure information preservation of the visual features after the encoding process, thus complicating the learning process of the quantum machine learning models. In particular, the problem, termed "Quantum Information Gap" (QIG), leads to a gap of information between classical and corresponding quantum features. We provide theoretical proof and practical demonstrations of that found and underscore the significance of QIG, as it directly impacts the performance of quantum machine learning algorithms. To tackle this challenge, we introduce a simple but efficient new loss function named Quantum Information Preserving (QIP) to minimize this gap, resulting in enhanced performance of quantum machine learning algorithms. Extensive experiments validate the effectiveness of our approach, showcasing superior performance compared to current methodologies and consistently achieving state-of-the-art results in quantum modeling.

Keywords: quantum information, quantum, clustering, transformer

1 Introduction

Quantum machine learning, as highlighted in [1–4], represents a promising research direction at the intersection of quantum computing and artificial intelligence. Within this realm, the utilization of quantum computers promises to significantly boost machine learning algorithms by leveraging their innate parallel attributes, thereby showcasing quantum advantages that surpass classical algorithms, as suggested by [5]. Due to the substantial collaborative endeavors of academia and industry, contemporary quantum devices, often referred to as noisy intermediate-scale quantum (NISQ) devices [6], are now capable of demonstrating quantum advantages in specific meticulously crafted tasks [7, 8]. An emerging research focus lies in leveraging near-term quantum devices for practical machine learning applications, with a prominent approach being hybrid quantum-classical algorithms [9, 10], also referred to as variational quantum algorithms. These algorithms typically employ a classical optimizer to refine quantum neural networks (QNNs), allocating complex tasks to quantum computers while assigning simpler ones to classical computers. In typical quantum machine learning scenarios, a quantum circuit utilized in variational quantum algorithms is commonly divided into two components: a data encoding circuit and a QNN. On the one hand, enhancing these algorithms’ efficacy in handling practical tasks involves the development of various QNN architectures. Numerous architectures, including strongly entangling circuit architectures [11], tree-tensor networks [12], quantum convolutional neural networks [13], and even automatically searched architectures [14–17], have been proposed. On the other hand, careful design of the encoding circuit is crucial, as it can significantly impact the generalization performance of these algorithms.

Encoding classical information into quantum data is a crucial step, as it directly impacts the performance of quantum machine learning algorithms. These algorithms are designed to optimize objective functions, such as classification, using encoded data. However, quantum encoding poses significant challenges, especially on near-term quantum devices, as highlighted in previous research [1]. While phase and amplitude encoding are foundational approaches, recent advancements have popularized parameterized quantum circuits (PQCs) as the most practical strategy for encoding on NISQ devices [18]. Nevertheless, despite the prevalence of PQCs, it is essential to utilize the basic encoding methods at the first step, such as phase and amplitude encoding. An important question arises regarding whether these encoding strategies guarantee preserving fundamental properties or characteristics of classical data in its quantum form.

Contributions of this Work: This paper has three key contributions. First, we identify a challenge with current visual encoding strategies regarding the preservation of information during the transition from classical to quantum data. Specifically, we observe distinct characteristics between feature spaces in quantum computing compared to their classical counterparts, resulting in lower performance of quantum machine learning algorithms than expected. Second, we introduce a simple but efficient novel training approach to generate classical features conducive to quantum machines post-encoding. This method holds promise for substantially enhancing quantum machine learning algorithms. Finally, our empirical experiments demonstrate the state-of-the-art performance of quantum machine learning across diverse benchmarks.

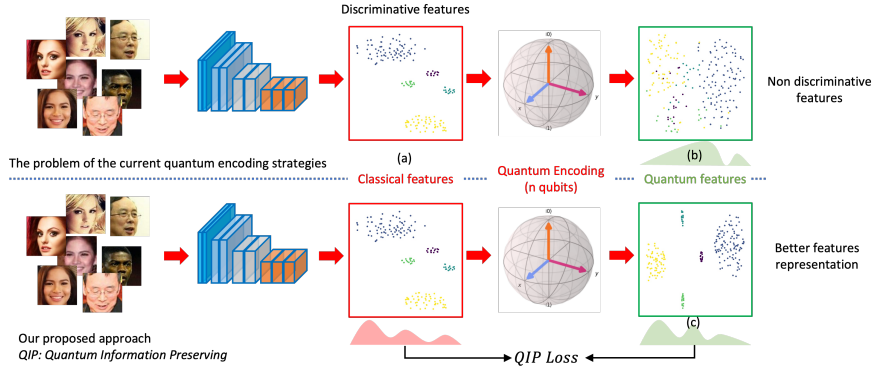


Fig. 1: Limitations in current quantum encoding strategies, which result in non-robust feature representations in the quantum feature space and our proposed QIP solution. Figure (b) showcases encoded quantum features. Figure (c) presents our proposed method for enhancing the discriminative of quantum features.

2 Related Work

2.1 Quantum Computer Vision

Several quantum techniques are available for computer vision tasks, such as recognition and classification [19, 20], object tracking [21], transformation estimation [22], shape alignment and matching [23–25], permutation synchronization [26], visual clustering [27], and motion segmentation [28]. Via Adiabatic Quantum Computing (AQC), O’Malley et al. [19] applied binary matrix factorization to extract features of facial images. In contrast, Li et al. [21] reduced redundant detections in multi-object detection. Dendukuri et al. [29] presented the image representation using quantum information to reduce the computational resources of classical computers. Cavallaro et al. [20] presented multi-spectral image classification using quantum SVM. Golyanik et al. [22] introduced correspondence problems for point sets using AQC to align the rotations between pairs of point sets. Meanwhile, [23] proposed a parameterized quantum circuit learning method for the point set matching problem. Using AQC to solve the formulated Quadratic Unconstrained Binary Optimization (QUBO), Nguyen et al. [27] proposed an unsupervised visual clustering method optimizing the distances between clusters. In contrast, Arrigoni et al. [28] optimized the matching motions of key points between consecutive frames.

2.2 Hybrid Classical-Quantum Machine Learning

Date et al. [30] implemented a classical high-performance computing model with an Adiabatic Quantum Processor for a classification task on the MNIST dataset. Their experiment evaluated two classification models, i.e., the Deep Belief Network (DBN) and the Restricted Boltzmann Machines (RBM). It is shown that classical computing performs heavy matrix computations efficiently while the sampling task is more convenient to quantum computing, as quantum mechanical processes are used to generate

samples, making them truly random. Barkoutsos et al. [31] introduced an improved platform for combinatorial optimization problems using hybrid classical-quantum variational circuits. It was empirically shown that this approach leads to faster convergence to better solutions for all combinatorial optimization problems on both classical simulation and quantum hardware. Romero et al. [32] presented generative modeling of continuous probability distributions via a Hybrid Quantum-Classical model. Inspired by convolutional neural networks, Liu et al. [33] proposed a hybrid quantum-classical convolutional neural network using the quantum advantage to enhance the feature mapping process, the most computationally intensive part of the convolutional neural networks. The feature map extracted by a parametrized quantum circuit can detect the correlations of neighboring data points in a complexly large space.

3 Background

3.1 Quantum Basics

In this section, we provide a concise introduction to fundamental concepts in quantum computing essential for this paper. For detailed comprehensive reviews, we refer to [34]. In quantum computing, quantum information is typically expressed through n -qubit (pure) quantum states within the Hilbert space \mathbb{C}^{2^n} . Specifically, a pure quantum state can be denoted by a unit vector $|\psi\rangle \in \mathbb{C}^{2^n}$ (or $\langle\psi|$), where the *ket* notation $|\psi\rangle$ signifies a column vector, and the *bra* notation $\langle\psi| = |\psi\rangle^\top$ with \top indicating the conjugate transpose, represents a row vector.

Mathematically, the evaluation of a pure quantum state $|\psi\rangle$ is delineated by employing a quantum circuit, often called a quantum gate. It is represented as $|\psi'\rangle = U|\psi\rangle$, where U denotes the unitary operator (matrix) signifying the quantum circuit, and $|\psi'\rangle$ represents the quantum state subsequent to the evolution. Standard single-qubit quantum gates encompass the Pauli operators.

$$X := \begin{bmatrix} 0 & 1 \\ 1 & 0 \end{bmatrix}, Y := \begin{bmatrix} 0 & -i \\ i & 0 \end{bmatrix}, Z := \begin{bmatrix} 1 & 0 \\ 0 & -1 \end{bmatrix}, \quad (1)$$

The corresponding rotation gates denoted by $R_P(\theta) = \exp(-i\theta P/2) = \cos\frac{\theta}{2}I - i\sin\frac{\theta}{2}P$, where the rotation angle $\theta \in [0, 2\pi)$ and $P \in \{X, Y, Z\}$ indicating rotation around X, Y, Z coordinates. In this paper, multiple-qubit quantum gates mainly include the identity gate I , the CNOT gate, and the tensor product of single-qubit gates, e.g., $Z \otimes Z$, $Z \otimes I$, $Z^{\otimes n}$ and so on.

Quantum measurement is a method for extracting classical information from a quantum state. For example, given a quantum state $|\psi\rangle$ and an observable H , one can design quantum measurements to obtain the information $\langle\psi|H|\psi\rangle$. This study concentrates on hardware-efficient Pauli measurements, where H is set as Pauli operators or their tensor products. For instance, one might choose $Z_1 = Z \otimes I^{\otimes(n-1)}$, $X_2 = I \otimes X \otimes I^{\otimes(n-2)}$, $Z_1Z_2 = Z \otimes Z \otimes I^{\otimes(n-2)}$, etc., with a total of n qubits.

3.2 Limitations in Current Quantum Encoding Methods

Let $\mathbf{v} \in \mathbb{R}^d$ be a typical d -dimension vector of a classical computer. We denote $\mathcal{E}(\mathbf{v})$ to be a quantum encoding function that transforms the vector \mathbf{v} into the vector $|\psi\rangle \in \mathbb{C}^{2^n}$ of quantum states over Hilbert space, where n is the number of qubits.

$$|\psi\rangle = \mathcal{E}(\mathbf{v}) \quad (2)$$

Specifically, the \mathcal{E} can be amplitude, phase encoding, or PQC. It is important to note that the $|\psi\rangle$ represents the qubits' states; for further usage of the quantum machine learning function, it is necessary to extract information from these quantum states. To accomplish it, the *observable* denoted as $\mathcal{O}(|\psi\rangle)$ is utilized. In particular, the observable \mathcal{O} measures the state of every single qubit. Let $\mathbf{q} = [q(0), \dots, q(i), \dots, q(n-1)] \in \mathbb{R}^n$ be a vector of information measured by \mathcal{O} where $q(i)$ is the measurement of i^{th} qubit and formulated as in Eqn. (3).

$$q(i) = \langle \psi | \mathcal{O}_i | \psi \rangle \quad (3)$$

In the equation above, a different observable \mathcal{O}_i is applied for each qubit. In particular, \mathcal{O}_i is a unitary operator represented by a matrix. Let P be a Pauli operation where $P \in \{X, Y, Z\}$, the \mathcal{O}_i can be further derived as Eqn. (4).

$$\mathcal{O}_i = I^{\otimes i} \otimes P \otimes I^{\otimes (n-i-1)} \quad (4)$$

According to Eqn. (4), we can measure the state of a qubit in any coordinates (X , Y , or Z) of the Hilbert space.

In summary, the relation between quantum information vector \mathbf{q} and classical information vector \mathbf{v} is represented as Eqn. (5).

$$\mathbf{v} \in \mathbb{R}^d \xrightarrow[\text{Quantum encoding}]{\mathcal{E}(\mathbf{v})} |\psi\rangle \in \mathbb{R}^{2^n} = \mathbb{R}^d \xrightarrow[\text{Measurement}]{\mathcal{O}(|\psi\rangle)} \mathbf{q} \in \mathbb{R}^n \quad (5)$$

Mathematically, we can define \mathcal{Q} as the function to map $\mathbf{v} \rightarrow \mathbf{q}$ as Eqn. (6).

$$\mathbf{q} = \mathcal{Q}(\mathbf{v}, \mathcal{E}, \mathcal{O}) \quad (6)$$

The details of the proposed framework are demonstrated in Fig. 2.

Proposition 1. Consider two different quantum state vectors, denoted as $|\psi_1\rangle$ and $|\psi_2\rangle$, and these corresponding quantum information vectors \mathbf{q}_1 and \mathbf{q}_2 . We have $\langle \psi_1 | \psi_2 \rangle \neq \mathbf{q}_1^T \mathbf{q}_2$ for any Pauli observable and quantum encoding strategies.

The proof can be found in the Supplementary section.

3.3 Theoretical Analysis and Problem Visualization

In this section, we first pre-define the definition of the term *information* as the correlation between pairwise vectors.

Theoretical Analysis. The goal of encoding \mathcal{E} is to transform a classical feature

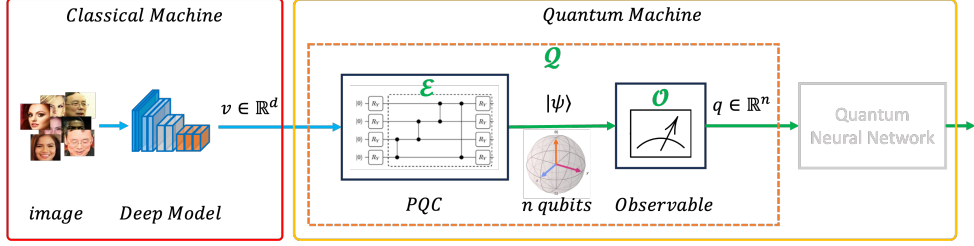


Fig. 2: Overview of the hybrid quantum system. The **red components** run in the classical machine. The **yellow box** includes components running on the quantum machine. The dashed **orange box** indicates our focus on this paper. **Best viewed in color.**

$\mathbf{v} \in \mathbb{R}^d$ into a quantum state $|\psi\rangle \in \mathbb{R}^d$ using fewer bits while retaining maximum information as much as in the classical one. Assuming \mathbf{v} is a normalized vector and \mathcal{E} represents an amplitude encoding, the preservation of information is evident as $\mathbf{v} = |\psi\rangle$. Additionally, since \mathcal{E} requires fewer than d qubits ($n < d$), it appears to be the optimal choice given these constraints.

However, the limitation of amplitude encoding is its potential unsuitability for many problems. To address this problem, Parametrized Quantum Circuits (PQC) have recently become the most prevalent encoding strategy. PQC incorporates trainable parameters that can be optimized during training, reducing dependencies on specific problems. However, information is not guaranteed to be preserved when representing features in Hilbert spaces of $|\psi\rangle$. Additionally, Proposition 2 suggests that no observables guarantee uniform discriminability between the features $|\psi\rangle$ and \mathbf{q} . Considering these factors, current encoding strategies fail to ensure the preservation of information when mapping classical features to quantum features, thus creating an information gap.

Looking at it from a different angle, if we temporarily set aside quantum theory, Eqn. (6) reveals that \mathcal{Q} serves as a dimension reduction function, mapping \mathbb{R}^d to \mathbb{R}^n where $n \ll d$. As far as we know, no flawless dimension reduction algorithms can preserve pairwise cosine distances between vectors. Even if a perfect algorithm existed, extending its theory to the quantum realm remains an open question.

Problem Visualization. Considering the task of face clustering [35], we assume that a model $\mathcal{M}(x)$ [36] is trained with metric loss functions [36, 37] to map a facial image x into a high-dimensional features space. This mapping ensures that similar faces are clustered closely while separating from faces of different identities. As discussed in [35], recent studies have significantly addressed large-scale clustering challenges within classical machine learning. These methods extensively utilize the discriminative nature of facial features, mainly relying on cosine distance in algorithmic design. However, envisioning a quantum counterpart algorithm that perfectly mirrors these methods reveals a crucial limitation. Despite their potential, quantum algorithms struggle to match the performance of classical ones due to the absence of ideal strategies for encoding classical information into quantum formats, as shown in the Proposition 2.

We illustrate the issue in Fig. 1 . Specifically, we employ a face recognition model, ResNet50 [38], trained with ArcFace [36] on the MSCeleb-1M database [39] using classical machine techniques. We randomly select subjects from the hold-out set and extract their facial features. Subsequently, we process the corresponding quantum information of these features according to Eqn. (5). The boundary between these subjects appears blurred in the quantum machine’s perspective, whereas it remains distinct in the classical one. Some samples close together in the classical machine space appear far apart in the quantum space, presenting challenges for quantum algorithms to determine the boundary.

4 Our Proposed Approach

4.1 Problem Formulation

Let $x \in \mathbb{R}^{h \times w \times c}$ denote the input image where h , w , and c are the image height, width, and number of channels correspondingly. Consider $\mathbf{v} = \mathcal{M}(x)$ is the deep features extracted by a model \mathcal{M} . Let \mathcal{K} be the function to measure the gap of information between classical vector \mathbf{v} and its corresponding quantum vector \mathbf{q} . Our goal can be presented as in Eqn. (7).

$$\min \mathcal{K}(\mathbf{v}, \mathbf{q}) = \mathcal{K}(\mathcal{M}(x), \mathcal{Q}(\mathcal{M}(x), \mathcal{E}, \mathcal{O})) \quad \text{w.r.t } \mathcal{E}, \mathcal{O} \quad \text{and } \mathbf{v} = \mathcal{M}(x) \quad (7)$$

4.2 Quantum Information Preserving Loss

In Eqn. (7), only \mathcal{M} and \mathcal{E} are considered trainable. Theoretically, we can optimize either \mathcal{M} or \mathcal{E} to minimize the Eqn. (7). In this study, however, we concentrate on training \mathcal{M} since, as demonstrated in Eqn. (5), $\mathbf{q} = \mathcal{M} \circ \mathcal{E} \circ \mathcal{O}$, indicating that \mathcal{M} initiates the quantum encoding process, making it the most critical component to address. Let \mathcal{F} represent the task-specific layer to train the feature representation of x . \mathcal{M} can be optimized with the objective function as in Eqn. (8).

$$\theta_{\mathcal{M}}^* = \arg \min_{\theta_{\mathcal{M}}} \mathbb{E}_{x_i \sim p(x_i)} [\mathcal{L}(\mathcal{F}(\mathcal{M}(x_i)), \hat{y}_i)] \quad (8)$$

Here, \hat{y}_i and \mathcal{L} denote the ground truth and the loss function, respectively. The common approach (e.g., [38, 40, 41]) typically designs \mathcal{F} as a fully connected layer and employs loss functions such as cross-entropy or metric losses (e.g., [36, 37]) for training a classification model. For simplicity, we choose cross-entropy as \mathcal{L} . It’s important to note that, however, \mathcal{L} is also applicable to metric loss functions like ArcFace or CosFace.

$$\mathcal{L} = -\frac{1}{N} \sum_{i=1}^N \log \frac{e^{W_{\hat{y}_i}^T \mathbf{v}_i + b_j}}{\sum_{j=1}^C e^{W_j^T \mathbf{v}_i + b_j}} \quad (9)$$

where $W_j \in \mathbb{R}^d$ denotes the j^{th} column of the weight $W \in \mathbb{R}^{d \times C}$. C is the number of classes and $b_j \in \mathbb{R}$ is the bias term. For simply, we fix $b_j = 0$ as in [37]. The equation turns out $\mathcal{L} = -\frac{1}{N} \sum_{i=1}^N \log \frac{e^{W_{\hat{y}_i}^T \mathbf{v}_i}}{\sum_{j=1}^C e^{W_j^T \mathbf{v}_i}}$. Interestingly, W_j represents a *center vector*

Algorithm 1 Pseudo-code for the implementation of Quantum Information Preserving Loss

Data:

$\{x_i\}_{i=1}^N \in \mathbb{R}^{N \times h \times w \times c}$: a set of N input images

$\{\hat{y}_i\}_{i=1}^N \in \mathbb{R}^N$: a set of N labels

\mathcal{M} : feature extractor

$\theta_{\mathcal{M}}$: trainable parameters of \mathcal{M}

$\lambda_{\mathcal{M}}$: learning rate of \mathcal{M}

λ : loss factor of Quantum Information Preserving loss

while *not convergent* **do**

$\mathbf{v}_i \leftarrow \mathcal{M}(x_i)$ // Extract classical features of the images

$\mathbf{q}_i \leftarrow \mathcal{Q}(\mathbf{v}_i, \mathcal{E}, \mathcal{O})$ // Transform into quantum features as Eqn. (6)

$S \leftarrow \mathcal{Q}(W, \mathcal{E}, \mathcal{O})$ // Transform into quantum center vectors

$\mathbf{w}_i \leftarrow \text{softmax}(W^\top \mathbf{v}_i)$ // Project classical features into logits

$\mathbf{u}_i \leftarrow \text{softmax}(S^\top \mathbf{q}_i)$ // Project quantum features into logits

$\mathcal{L} \leftarrow \frac{1}{N} \sum_{i=1}^N -\log w_{i, \hat{y}_i}$ // Apply metric loss as Eqn. (9)

$\mathcal{K} \leftarrow \frac{1}{N} \sum_{i=1}^N \sum_{j=1}^C w_{i,j} \log \frac{w_{i,j}}{u_{i,j}}$ // Apply KL divergence as Eqn. (10)

$\mathcal{L}_{\text{QIP}} \leftarrow \mathcal{L} + \lambda \mathcal{K}$ // Compute the Quantum Information Preserving Loss

$\theta_{\mathcal{M}} \leftarrow \theta_{\mathcal{M}} - \lambda_{\mathcal{M}} \nabla_{\theta_{\mathcal{M}}} \mathcal{L}_{\text{QIP}}$ // Do backpropagation

end

corresponding to class j . The loss function \mathcal{L} optimizes model \mathcal{M} so that the vector \mathbf{v}_i aligns closely with W_j if they belong to the same class in the feature space. Moreover, $W_j^\top \mathbf{v}$ signifies the cosine distance between the two vectors since as in [36, 37] these features are normalized, which precisely fulfills the roles of $|\psi_1\rangle$ and $|\psi_2\rangle$ in Proposition 2. Leveraging this elegant property, we can define \mathcal{K} as the Kullback-Leibler divergence (KL) to minimize the information gap as formulated in Eqn. (7) as follows:

$$\begin{aligned} \mathcal{K} &= \frac{1}{N} \sum_{i=1}^N \text{KL}(W^\top \mathbf{v}_i, S^\top \mathbf{q}_i) \\ &= \frac{1}{N} \sum_{i=1}^N \sum_{j=1}^C \text{softmax}(W^\top \mathbf{v}_i)_j \times \log \frac{\text{softmax}(W^\top \mathbf{v}_i)_j}{\text{softmax}(S^\top \mathbf{q}_i)_j} \end{aligned} \quad (10)$$

where S_j is the corresponding quantum information vector of W_j using Eqn. (6). In conclusion, we propose a novel loss function named Quantum Information Preserving Loss to train \mathcal{M} as follows:

$$\theta_{\mathcal{M}}^* = \arg \min_{\theta_{\mathcal{M}}} \mathbb{E}_{x_i \sim p(x_i)} \left[-\log \frac{e^{W_{\hat{y}_i}^\top \mathbf{v}_i}}{\sum_{j=1}^C e^{W_j^\top \mathbf{v}_i}} + \lambda \times \text{KL}(W^\top \mathbf{v}_i, S^\top \mathbf{q}_i) \right] \quad (11)$$

where λ is the loss factor for controlling how much information is preserved. Using this loss function, the model \mathcal{M} can produce the feature \mathbf{v} , which is *friendly* with the quantum machine by keeping as much information after the quantum encoding. We also provide the pseudo-code in the Algorithm 1.

5 Experiment Setup and Implementation

Given that Proposition 2 implies the information as the relationship between two vectors, i.e., cosine similarity, selecting the model \mathcal{M} optimized for cosine similarity becomes paramount for problem validation and experimental demonstration. Consequently, this study aims for unsupervised clustering tasks, namely face and landmark clustering, as they align well with models trained using cosine-based loss functions. It is important to note that similar problems, such as classification, also apply to our proposed Proposition 2.

5.1 Experiment Setup

We follow the experimental framework outlined in previous studies [35, 42–48]. In essence, our clustering methodology consists of three key stages. First, we train a model $\mathcal{M}(x)$ to extract image features x . Second, the k nearest neighbors algorithm, denoted as $\mathbf{K}(x_i, k)$, is utilized to identify the k most similar neighbors of a given sample x_i , forming a cluster $\Phi_i = \mathbf{K}(x_i, k)$. Finally, as clusters Φ_i may encompass erroneous samples due to challenges such as database anomalies or imperfect feature representations by \mathcal{M} , previous studies have proposed training a model $\mathcal{N}(\Phi_i)$ to detect and eliminate these inaccuracies, thereby refining the cluster.

In contrast to prior research, we focus on studying this problem from a quantum perspective. It leads to designing modules, namely $\mathcal{M}(x)$ and $\mathcal{N}(\Phi_i)$, to operate on quantum hardware to the fullest extent possible. While training $\mathcal{M}(x)$ using our proposed methodology constitutes a critical aspect of this study, We aim to design $\mathcal{N}(\Phi_i)$ as a quantum machine learning model, thus enabling the entire pipeline to be executed on a quantum machine as much as possible.

Multiple methodologies have addressed the clustering problem on classical computers. These include traditional techniques [49, 50], graph-based methodologies [42–46, 51], and transformer-based approaches [35]. While transformer architectures have demonstrated significant success in various computer vision tasks [35, 48, 52–65], their potential in quantum computing remains promising. Adapting the typical transformer architecture for quantum systems, as proposed by [66], offers added convenience. Although graph-based networks present a possible option, the computational challenge of processing large datasets, such as a $(5.2\text{M} \times 5.2\text{M})$ sparse matrix on a quantum machine or even a simulated one, poses limitations. In contrast, transformer models do not encounter such constraints. Hence, inspired by the insights from [35], we propose redesigning $\mathcal{N}(\Phi_i)$ as a transformer-based quantum model.

5.2 Implementation Details

We employ ResNet50 architecture to train the model $\mathcal{M}(x)$ as prior works [35, 43, 51]. This model is trained on large-scale datasets like MSCeleb-1M, employing ArcFace [36] for feature representation learning. In addition to ArcFace, we integrate the Quantum Information Preserving Loss outlined in Section 4 to mitigate information loss during encoding. The loss factor λ is configured at 0.5.

To implement the Quantum Clusformer $\mathcal{N}(\Phi_i)$, we initially redesign the self-attention layer [67] tailored for quantum machines. We employ Parameterized

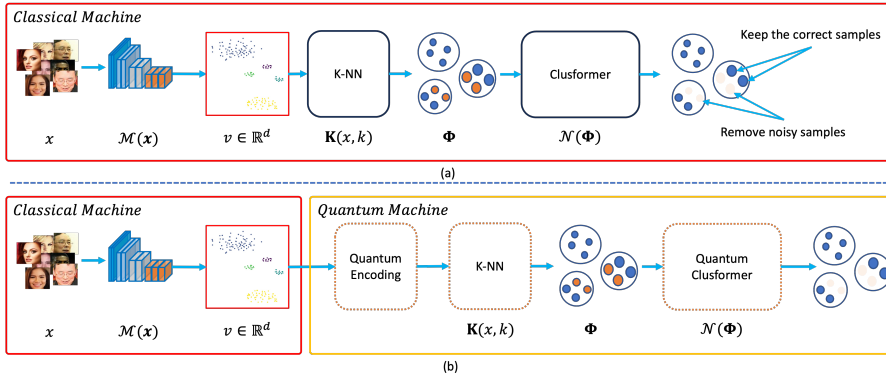


Fig. 3: Experiment setup and objective of the clustering problem. Figure (a) depicts the typical experiment setup used by [35] for the classical machine. Figure (b) shows a similar setup. However, only deep model $\mathcal{M}(x)$ retains running on the classical machine, while the rest of the modules are redesigned to run on the quantum computer.

Quantum Circuits (PQC) for each Query, Key, and Value layer. We construct transformer blocks suitable for the transformer-based model. Ultimately, we achieve full implementation of the Quantum Clusformer on quantum machines.¹

For the components running on the classical machine, we use the PyTorch framework while we utilize the torchquantum library [68] and cuQuantum to simulate the quantum machine. Since this library relays Pytorch as the backend, we can also leverage GPUs and CUDA to speed up the training process. The models are trained utilizing an $8 \times$ A100 GPU setup, each with 40GB of memory. The learning rate is initially set to 0.0001, progressively decreasing to zero following the CosineAnnealing policy [69]. Each GPU operates with a batch size of 512. The optimization uses AdamW [70] for 12 epochs. Training time for the model \mathcal{M} is approximately 2 hours, and the training time for the Quantum Clusformer $\mathcal{N}(\Phi_i)$ is about 4 hours.

5.3 Datasets and Metrics

We follow [42, 43] to use MSCeleb-1M [39] and [35] to use the Google Landmarks Dataset Version 2 (GLDv2) [71] for experiments. The Fig. 4 demonstrates samples from these datasets. For the evaluation metrics and protocols, we also follow the standard benchmarks from the previous studies [35, 42, 43, 47, 51]. We refer to the Supplementary of this work for the details of our experimental setup and datasets.

6 Experimental Results

6.1 Performance on MSCeleb-1M Clustering

The performance of our proposed method is shown in the Table 1. To begin, we define QClusformer as the Clusformer operating on a quantum machine for ease of

¹Code will be released upon acceptance

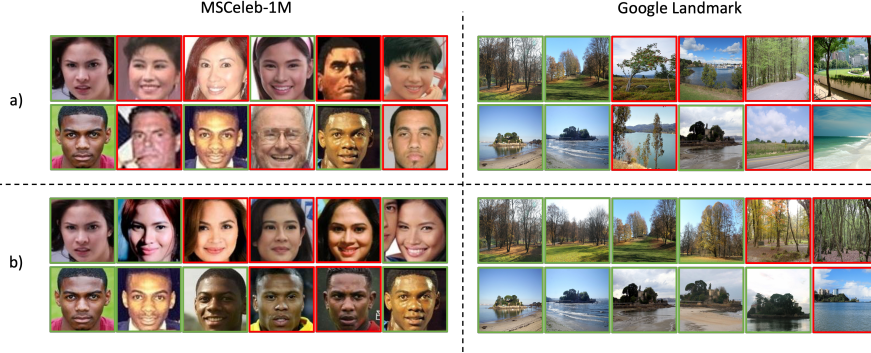


Fig. 4: The MSCeleb-1M and Google Landmark datasets are illustrated through samples. Each row represents either a subject (for MSCeleb-1M) or a location (for Google Landmark). The first image in each row denotes the center of a cluster Φ_i , while the subsequent images are the nearest neighbors of the first one, identified through the K-NN algorithm utilizing quantum features. Images bordered in red signify that they belong to a different class than the first image in the row, whereas those bordered in green share the same class as the first image. The clusters obtained without QIP loss in (a) exhibit more noisy samples compared to (b), which are obtained with QIP Loss. **Best view in color.**

reference. However, due to hardware constraints, we can only emulate QClusformer with fewer layers/transformer blocks than the original model [35]. To ensure a fair evaluation, we initially retrain the Clusformer, denoted as Clusformer[†], on a classical machine using identical configurations to those of QClusformer, explicitly setting the number of encoders to 1. The training process is outlined in Fig. 3(a). As a result, the performance of Clusformer[†] is slightly inferior to the original model. Notably, the F_P metric decreases from 88.20% to 86.49% on the 584K test set, representing an approximate 2% reduction. It consistently maintains marginally lower performance across both F_B and F_P on the remaining test sets.

Then, we train QClusformer with the strategy as in Fig. 3(b). Our chosen encoding strategy is amplitude, paired with Pauli-Z as the observable for the baseline. There is a notable decline in performance, approximately 2.8%. However, employing the QIP Loss function within the same setup is a potent remedy for bridging the information gap between quantum and classical features, resulting in a notable performance recovery. Noted that QClusformer with QIP Loss achieves 87.18% and 91.01% on F_P and F_B , respectively, on the 584K test set, surpassing Clusformer[†] by 0.6% and 3.2%, respectively. Similar trends are observed across all test sets of MSCeleb-1M.

These findings underscore the competitive performance of Quantum Clusformer, particularly when leveraging with QIP Loss. Notably, its performance surpasses that of the best-performing Clusformer with a complete setup on a classical machine, signaling the promising capabilities of quantum computing in the clustering problem.

6.2 Performance on Google-Landmark Clustering

Table 1: Performance on face clustering w.r.t the different number of unlabeled test sets. The terms *Enc* and *Obs* represent quantum encoding strategies and observables, respectively. The *A* and *Z* are amplitude encoding and Pauli-Z observables, correspondingly. QIP is representing for Quantum Information Preserving Loss.

| Compute Type | Num. unlabeled | Setup | | 584K | | 1.74M | | 2.89M | | 4.05M | | 5.21M | |
|--------------|-------------------------|-------|-----|--------------|--------------|--------------|--------------|--------------|--------------|--------------|--------------|--------------|--------------|
| | Method / Metrics | Enc | Obs | F_P | F_B | F_P | F_B | F_P | F_B | F_P | F_B | F_P | F_B |
| Classical | K-means [72, 73] | - | - | 79.21 | 81.23 | 73.04 | 75.2 | 69.83 | 72.34 | 67.90 | 70.57 | 66.47 | 69.42 |
| | HAC [74] | - | - | 70.63 | 70.46 | 54.40 | 69.53 | 11.08 | 68.62 | 1.40 | 67.69 | 0.37 | 66.96 |
| | DBSCAN [49] | - | - | 67.93 | 67.17 | 63.41 | 66.53 | 52.50 | 66.26 | 45.24 | 44.87 | 44.94 | 44.74 |
| | ARO [50] | - | - | 13.60 | 17.00 | 8.78 | 12.42 | 7.30 | 10.96 | 6.86 | 10.50 | 6.35 | 10.01 |
| | CDP [75] | - | - | 75.02 | 78.70 | 70.75 | 75.82 | 69.51 | 74.58 | 68.62 | 73.62 | 68.06 | 72.92 |
| | L-GCN [51] | - | - | 78.68 | 84.37 | 75.83 | 81.61 | 74.29 | 80.11 | 73.70 | 79.33 | 72.99 | 78.60 |
| | LTC [42] | - | - | 85.66 | 85.52 | 82.41 | 83.01 | 80.32 | 81.10 | 78.98 | 79.84 | 77.87 | 78.86 |
| | GCN-V [43] | - | - | 87.14 | 85.82 | 83.49 | 82.63 | 81.51 | 81.05 | 79.97 | 79.92 | 78.77 | 79.09 |
| | GCN-VE [43] | - | - | 87.93 | 86.09 | 84.04 | 82.84 | 82.10 | 81.24 | 80.45 | 80.09 | 79.30 | 79.25 |
| | Clusformer [35] | - | - | 88.20 | 87.17 | 84.60 | 84.05 | 82.79 | 82.30 | 81.03 | 80.51 | 79.91 | 79.95 |
| | Pair-Cls [76] | - | - | 90.67 | 89.54 | 86.91 | 86.25 | 85.06 | 84.55 | 83.51 | 83.49 | 82.41 | 82.40 |
| | STAR-FC [46] | - | - | 91.97 | - | 88.28 | 86.26 | 86.17 | 84.13 | 84.70 | 82.63 | 83.46 | 81.47 |
| | Ada-NETS [47] | - | - | 92.79 | 91.40 | 89.33 | 87.98 | 87.50 | 86.03 | 85.40 | 84.48 | 83.99 | 83.28 |
| | LCE-PCENet [45] | - | - | 94.64 | 93.36 | 91.90 | 90.78 | 90.27 | 89.28 | 88.69 | 88.15 | 87.35 | 87.28 |
| | CLIP-Cluster [44] | - | - | - | - | 91.44 | 89.44 | 89.95 | 87.75 | 88.93 | 86.78 | 87.99 | 85.85 |
| | Clusformer [†] | - | - | 86.49 | 89.82 | 84.40 | 87.84 | 82.41 | 85.86 | 80.42 | 83.87 | 78.33 | 81.73 |
| Quantum | QClusformer | A | Z | 83.68 | 86.89 | 81.93 | 85.19 | 79.77 | 83.05 | 78.32 | 81.41 | 76.15 | 79.29 |
| | QClusformer + QIP Loss | A | Z | 87.18 | 91.01 | 85.14 | 89.32 | 83.19 | 87.34 | 81.59 | 85.83 | 79.40 | 83.78 |

In this section, we compare the proposed method’s performance on the Google Landmark dataset, a visual landmark clustering dataset shown in Table 2. The experimental setups and evaluation protocols are similar to the previous MSCeleb-1M section and in the prior work, [35]. Similar results to those obtained with the MSCeleb-1M database are observed. Specifically, Clusformer[†], when runs on a classical machine, achieves 17.74% and 38.80% in terms of F_P and F_B respectively. However, when the model operates on a quantum machine named QClusformer, there is a significant performance drop from 13.20% to 35.63% for F_P and F_B , respectively. Nonetheless, by using the QIP Loss function, the performance rebounds to 19.02% for F_P and 40.28% for F_B , surpassing that of Clusformer[†] and remaining competitive with the original Clusformer which has 19.32% and 40.63% of F_P and F_B .

6.3 Ablation Studies

This ablation study section is used to practically prove the Proposition 2.

QIP Works With Different Encoding Strategies. In Proposition 2, we present the information gap between quantum and classical machines across various encoding strategies. To demonstrate the efficiency of our proposed method with diverse encoding approaches, we initially hold observables constant, specifically the Pauli-Z,

Table 2: Performance on landmark clustering w.r.t different quantum encoding and observables.

| Compute Type | Methods | Enc | Obs | F_P | F_B |
|--------------|-------------------------|-----|-----|--------------|--------------|
| Classical | K-means [72, 73] | - | - | 8.52 | 14.02 |
| | HAC [74] | - | - | 0.2 | 20.88 |
| | DBSCAN [49] | - | - | 0.97 | 17.38 |
| | Spectral [77] | - | - | 6.93 | 18.28 |
| | ARO [50] | - | - | 0.32 | 10.54 |
| | L-GCN [51] | - | - | 14.08 | 36.35 |
| | GCN-V [43] | - | - | 16.1 | 34.86 |
| | GCN-VE [43] | - | - | 10.2 | 30.23 |
| | Clusformer [35] | - | - | 19.32 | 40.63 |
| | Clusformer [†] | - | - | 17.74 | 38.80 |
| Quantum | QClusformer | A | Z | 13.20 | 35.63 |
| | QClusformer + QIP Loss | A | Z | 19.02 | 40.28 |

Table 3: Ablation studies on different encoding strategies.

| | | Num. unlabeled | | Setup | | 584K | |
|---------|-------------------------|------------------|---|--------------|--------------|-------|-------|
| | | Method / Metrics | | Enc Obs | | F_P | F_B |
| Cls | Clusformer [35] | - | - | 88.20 | 87.17 | | |
| | Clusformer [†] | - | - | 86.49 | 89.82 | | |
| Quantum | QClusformer | A | Z | 83.68 | 86.89 | | |
| | QClusformer + QIP Loss | A | Z | 87.18 | 91.01 | | |
| | QClusformer + QIP Loss | P | Z | 86.42 | 88.41 | | |
| | QClusformer + QIP Loss | U | Z | 85.20 | 89.64 | | |

Table 4: Ablation studies on different observables.

| | | Num. unlabeled | | Setup | | 584K | |
|---------|-------------------------|------------------|----|--------------|--------------|-------|-------|
| | | Method / Metrics | | Enc Obs | | F_P | F_B |
| Cls | Clusformer [35] | | | 88.20 | 87.17 | | |
| | Clusformer [†] | | | 86.49 | 89.82 | | |
| Quantum | QClusformer | A | Z | 83.68 | 86.89 | | |
| | QClusformer + QIP Loss | A | Z | 87.18 | 91.01 | | |
| | QClusformer + QIP Loss | A | X | 86.40 | 90.30 | | |
| | QClusformer + QIP Loss | A | XZ | 86.74 | 89.28 | | |
| | QClusformer + QIP Loss | U | Z | 85.20 | 89.64 | | |
| | QClusformer + QIP Loss | U | Y | 84.35 | 90.54 | | |

and subsequently change between phase and U_3 encoding [18]. Unlike amplitude and phase encoding, U_3 represents a Parameterized Quantum Circuit (PQC) with trainable parameters. The performances of these configurations are detailed in Table 5. Remarkably, the QClusformer, trained with QIP Loss, the Pauli-Z observable, and either phase or U_3 encoding strategies, consistently outperforms the standalone QClusformer. It underscores the adaptability of the QIP Loss across diverse encoding strategies. Notably, phase and U_3 encoding show inferior performance compared to amplitude. As we mentioned in the previous section, the amplitude is naturally fit for the clustering problem than other strategies.

QIP Works With Different Observables. The intuition of these ablation studies is similar to the encoding above strategies. In particular, we fix the encoding strategies as amplitude while experimenting with various observables, i.e., Z , X , and XZ (a combination of measuring both X and Z coordinates). As depicted in Table 6, QClusformer exhibits the highest accuracy in F_P and F_B when utilizing the Z observable, while both X and XZ show slight decreases. When dealing with the Pauli-Y observable, amplitude strategies prove ineffective as they result in all-zero measurements. Consequently, we select U_3 for encoding and compare the performance of Pauli-Y versus Pauli-Z. Interestingly, the performance using Pauli-Y remains relatively unchanged compared to Pauli-Z. Nonetheless, these configurations still significantly outperform QClusformer alone, underscoring the versatility of the Quantum Information Processing (QIP) approach across diverse observables.

The role of λ - QIP Loss Factor. We investigate the impact of the control factor λ for managing QIP Loss on the performance. To achieve this, we conduct experiments using a subset of 584K samples from the MSCeleb-1M dataset. The experimental configurations remain consistent with those outlined in the previous section, i.e., employing amplitude encoding and Pauli-Z observable.

The results are shown in Fig. 5. When $\lambda = 0$, indicating the absence of QIP Loss utilization, the performance stands at 83.68% and 86.89% for F_P and F_B respectively, as detailed in Table 1 above. Gradually increasing this parameter yields a steady enhancement in performance. However, the peak performance is attained at $\lambda = 0.5$, after which a decline is observed. This phenomenon is due to the role of QIP Loss in minimizing the disparity between quantum and classical features. According to Proposition 2, the gap towards zero only when two vectors \mathbf{v}_1 and \mathbf{v}_2 are identical. In

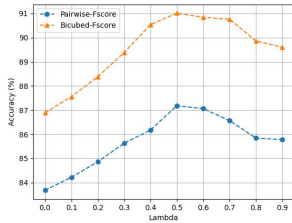


Fig. 5: Ablation studies on different QIP Loss factor λ

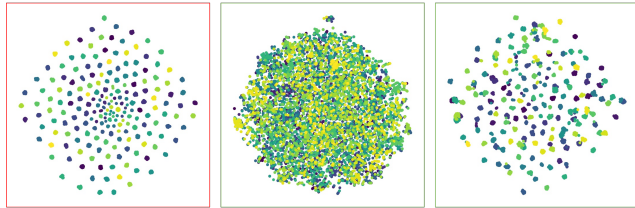


Fig. 6: Ablation studies on features representation using QIP Loss. From left to right, the first image presents classical features, the second one presents quantum features w/o QIP Loss, and the last one shows the quantum features optimized by QIP Loss.

this case, the model \mathcal{M} generates similar features irrespective of input images, leading to model collapse and failure in distinguishing samples from distinct classes. Hence, it is necessary to control λ to prevent such collapse. Our investigation found that the optimal value for λ within this framework is 0.5.

Quantum Feature Representations. We investigate how QIP Loss helps to align the features in the quantum computer as in Fig. 6. We randomly select 200 subjects from 581K part of MSCeleb-1M to extract the features. We employ T-SNE to reduce the dimension from 256 to 2 and visualize these features in the 2D space. From left to right, the first image (with a red border) indicates the classical features. The second image (with a green border) illustrates the quantum features of these subjects without training with QIP Loss, and the last one demonstrates the quantum features optimized by QIP Loss.

7 Conclusion

This paper revisits the quantum visual feature encoding strategies employed in quantum machine learning with computer vision applications. We identify a significant Quantum Information Gap (QIG) issue stemming from current encoding methods, resulting in non-discriminative feature representations in the quantum space, thereby challenging quantum machine learning algorithms. To tackle this challenge, we propose a simple yet effective solution called Quantum Information Preserving Loss. Through empirical experiments conducted on various large-scale datasets, we demonstrate the effectiveness of our approach, achieving state-of-the-art performance in clustering problems on quantum machines. Our insights into quantum encoding strategies are poised to stimulate further research efforts in this domain, prompting researchers to focus on designing more effective quantum machine learning algorithms.

8 Discussion

Since quantum machines have limited access to the general public, the experiments were carried out through noise-free simulation systems such as torchquantum and

Quantum. However, real-world scenarios may involve noise within the system, leading to uncertain quantum state measurements and affecting overall performance. Despite this limitation, the theoretical problem of QIG persists. It is crucial to figure out that quantum machine learning algorithms must confront these dual challenges of QIP and noise. We anticipate that addressing these issues will attract significant research attention in future endeavors.

9 Supplementary information

9.1 Proof of Proposition 1

Proposition 2. *Consider two different quantum state vectors, denoted as $|\psi_1\rangle$ and $|\psi_2\rangle$, and these corresponding quantum information vectors \mathbf{q}_1 and \mathbf{q}_2 . We have $\langle\psi_1|\psi_2\rangle \neq \mathbf{q}_1^\top \mathbf{q}_2$ for any Pauli observable and quantum encoding strategies.*

Proof. As $q(i) = \langle\psi|\mathcal{O}_i|\psi\rangle$, we have:

$$\begin{aligned}
\mathbf{q}_1^\top \mathbf{q}_2 &= \sum_{i=1}^n q_1(i)q_2(i) \\
&= \sum_{i=1}^n \langle\psi_1|\mathcal{O}_i|\psi_1\rangle \langle\psi_2|\mathcal{O}_i|\psi_2\rangle \\
&= \langle\psi_1| \left(\sum_{i=1}^n \mathcal{O}_i |\psi_1\rangle \langle\psi_2|\mathcal{O}_i \right) |\psi_2\rangle, \\
&= \langle\psi_1|A|\psi_2\rangle,
\end{aligned} \tag{12}$$

where $A = \sum_{i=1}^n (\mathcal{O}_i |\psi_1\rangle \langle\psi_2|\mathcal{O}_i)$. We have to prove that $A \neq I$. That is true because:

$$\begin{aligned}
\text{tr}(A) &= \sum_{i=1}^n \text{tr}(\mathcal{O}_i |\psi_1\rangle \langle\psi_2|\mathcal{O}_i) \\
&= \sum_{i=1}^n \text{tr}(\mathcal{O}_i \mathcal{O}_i |\psi_1\rangle \langle\psi_2|) \\
&= \sum_{i=1}^n \text{tr}(|\psi_1\rangle \langle\psi_2|)
\end{aligned} \tag{13}$$

From Proposition 2, since $|\psi_1\rangle \neq |\psi_2\rangle$, then $\langle\psi_1|\psi_2\rangle = \text{tr}(|\psi_1\rangle \langle\psi_2|) < 1$. For that reason, we have $\text{tr}(A) < n$ then $A \neq I$ since $\text{tr}(I) = n$. The proposition 2 has been proven. \square

9.2 Datasets and Metrics

Datasets. MSCeleb-1M [39] is a vast face recognition dataset compiled from web sources, encompassing 100,000 identities, with each identity represented by approximately 100 facial images. Nonetheless, the original dataset retains noisy labels. Consequently, we utilize a subset derived from ArcFace [36], which undergoes improved annotation post-cleaning. This refined dataset comprises 5.8 million images sourced from 85,000 identities. All images undergo preprocessing, involving alignment and cropping to dimensions of 112×112 .

The Google Landmarks Dataset Version 2 (GLDv2) [71] is one of the largest datasets dedicated to visual landmark recognition and identification. Its cleaned iteration comprises 1.4 million images spanning 85,000 landmarks and 800 hours of human annotation. These landmarks span diverse categories and are sourced from various corners of the globe. The dataset exhibits an extremely long-tail distribution, with the number of images per class varying from 0 to 10,000. Compared to face recognition tasks, GLDv2 presents a similar yet notably more challenging scenario. We randomly partition the dataset into three segments, each featuring 28,000 landmarks. Notably, there is no overlap between these partitions. One segment is designated for training the deep visual model and Clusformer, while the remaining segments are reserved for testing purposes.

Metrics. To evaluate the approach for the clustering task, we follow [35, 42, 43] and use Fowlkes Mallows Score to measure the similarity between two clusters with a set of points. This score is computed by taking the geometry mean of precision and recall of the point pairs. Thus, Fowlkes Mallows Score is called Pairwise F-score (F_P). BCubed F-score F_B is another popular metric for clustering evaluation focusing on each data point.

9.3 Ablation Studies

9.3.1 Full Results on Different Encoding Strategies of the MSCeleb-1M

Table 5 shows the extended results on the five test sets of face clustering with different encoding strategies, i.e., amplitude encoding, phase encoding, and U_3 encoding.

Table 5: Ablation studies on different encoding strategies of the MSCeleb-1M.

| Num. unlabeled | | Setup | 584K | | 1.74M | | 2.89M | | 4.05M | | 5.21M | | |
|------------------|-------------------------|-------|------|--------------|--------------|--------------|--------------|--------------|--------------|--------------|--------------|--------------|--------------|
| Method / Metrics | | Enc | Obs | F_P | F_B | F_P | F_B | F_P | F_B | F_P | F_B | F_P | F_B |
| Cls | Clusformer [35] | - | - | 88.20 | 87.17 | 84.60 | 84.05 | 82.79 | 82.30 | 81.03 | 80.51 | 79.91 | 79.95 |
| | Clusformer [†] | - | - | 86.49 | 89.82 | 84.40 | 87.84 | 82.41 | 85.86 | 80.42 | 83.87 | 78.33 | 81.73 |
| Quantum | QClusformer | A | Z | 83.68 | 86.89 | 81.93 | 85.19 | 79.77 | 83.05 | 78.32 | 81.41 | 76.15 | 79.29 |
| | QClusformer + QIP Loss | A | Z | 87.18 | 91.01 | 85.14 | 89.32 | 83.19 | 87.34 | 81.59 | 85.83 | 79.40 | 83.78 |
| | QClusformer + QIP Loss | P | Z | 86.42 | 88.41 | 84.73 | 86.60 | 82.82 | 84.62 | 81.36 | 83.06 | 79.33 | 81.01 |
| | QClusformer + QIP Loss | U_3 | Z | 85.20 | 89.64 | 83.68 | 87.71 | 81.49 | 85.62 | 80.03 | 83.73 | 77.84 | 81.79 |

9.3.2 Full Results on Different Observables of the MSCeleb-1M

Table 6 illustrates the extended results on the five test sets of face clustering with different observables. For the amplitude encoding, we use observables Z , X , and their combination to measure. And we use observables Z and Y for the U_3 encoding. As the amplitude encoding represents the quantum state as real numbers and the observable Y measures on the imaginary numbers axis that makes the measurement all zeros, we ignore this setting. Note that this setting still holds our proposition.

Table 6: Ablation studies on different observables of MSCeleb-1M.

| Num. unlabeled | | Setup | 584K | | 1.74M | | 2.89M | | 4.05M | | 5.21M | |
|------------------|-------------------------|---------|--------------|--------------|--------------|--------------|--------------|--------------|--------------|--------------|--------------|--------------|
| Method / Metrics | | Enc Obs | F_P | F_B | F_P | F_B | F_P | F_B | F_P | F_B | F_P | F_B |
| Cls | Clusformer [35] | - - | 88.20 | 87.17 | 84.60 | 84.05 | 82.79 | 82.30 | 81.03 | 80.51 | 79.91 | 79.95 |
| | Clusformer [†] | - - | 86.49 | 89.82 | 84.40 | 87.84 | 82.41 | 85.86 | 80.42 | 83.87 | 78.33 | 81.73 |
| Quantum | QClusformer | A Z | 83.68 | 86.89 | 81.93 | 85.19 | 79.77 | 83.05 | 78.32 | 81.41 | 76.15 | 79.29 |
| | QClusformer + QIP Loss | A Z | 87.18 | 91.01 | 85.14 | 89.32 | 83.19 | 87.34 | 81.59 | 85.83 | 79.40 | 83.78 |
| | QClusformer + QIP Loss | A X | 86.40 | 90.30 | 84.32 | 88.76 | 82.40 | 86.85 | 80.95 | 85.27 | 79.03 | 83.29 |
| | QClusformer + QIP Loss | A XZ | 86.74 | 89.28 | 84.79 | 87.23 | 82.58 | 85.02 | 81.17 | 83.49 | 79.03 | 81.50 |
| | QClusformer + QIP Loss | U_3 Z | 85.20 | 89.64 | 83.68 | 87.71 | 81.49 | 85.62 | 80.03 | 83.73 | 77.84 | 81.79 |
| | QClusformer + QIP Loss | U_3 Y | 84.35 | 90.54 | 82.45 | 88.96 | 80.27 | 86.97 | 78.50 | 85.06 | 76.46 | 83.07 |

9.3.3 Full Results of the Google Landmark Clustering

Table 7 presents the results of the Google Landmark Clustering with extended settings. We evaluate the method with different encoding strategies, i.e., amplitude encoding, phase encoding, and U_3 encoding, and different Pauli observables.

9.4 Details of the U_3 encoding

Fig. 7 demonstrates the structure of U_3 encoding. After encoding the classical feature \mathbf{v} into a quantum state, we use U_3 circuit, i.e., rotating operators in three axes X, Y, and Z, to transform the state. We define $\theta_i \in \mathbb{R}^3$ as a trainable vector containing three rotation values. For every layer of the U_3 circuit, entanglements are used to enhance the correlation between qubits.

9.5 Details of Quantum Clusformer Framework

Given a cluster Φ , we build Quantum Clusformer Framework $\mathcal{N}(\Phi)$ based on [35] as shown in Fig. 8. As the limitation of computational resources, we use one layer of quantum transformer block to find the hard samples, i.e., the samples having different classes from the center of the cluster.

References

- [1] Biamonte, J., Wittek, P., Pancotti, N., Rebentrost, P., Wiebe, N., Lloyd, S.: Quantum machine learning. *Nature* **549**(7671), 195–202 (2017)

Table 7: Performance on landmark clustering w.r.t different quantum encoding and observables.

| Compute Type | Methods | Enc | Obs | F_P | F_B |
|------------------------|-------------------------|----------------|-------|--------------|--------------|
| Classical | K-means [72, 73] | - | - | 8.52 | 14.02 |
| | HAC [74] | - | - | 0.2 | 20.88 |
| | DBSCAN [49] | - | - | 0.97 | 17.38 |
| | Spectral [77] | - | - | 6.93 | 18.28 |
| | ARO [50] | - | - | 0.32 | 10.54 |
| | L-GCN [51] | - | - | 14.08 | 36.35 |
| | GCN-V [43] | - | - | 16.1 | 34.86 |
| | GCN-VE [43] | - | - | 10.2 | 30.23 |
| | Clusformer [35] | - | - | 19.32 | 40.63 |
| | Clusformer [†] | - | - | 17.74 | 38.80 |
| Quantum | QClusformer | A | Z | 13.20 | 35.63 |
| | QClusformer + QIP Loss | A | Z | 19.02 | 40.28 |
| | QClusformer + QIP Loss | A | X | 18.50 | 38.86 |
| | QClusformer + QIP Loss | A | XZ | 17.58 | 37.84 |
| | QClusformer + QIP Loss | P | Z | 17.02 | 36.50 |
| | QClusformer + QIP Loss | U ₃ | Z | 16.64 | 36.04 |
| QClusformer + QIP Loss | U ₃ | Y | 16.41 | 36.68 | |

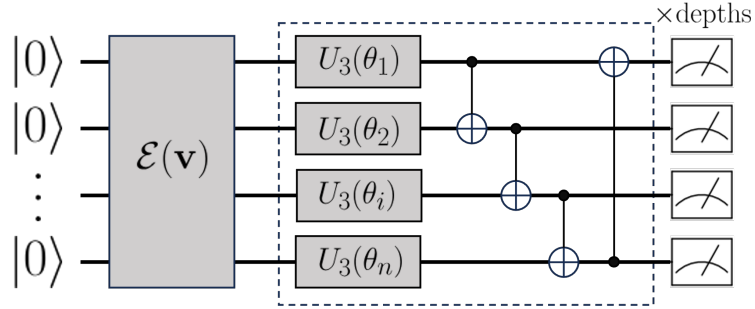


Fig. 7: Parameterized Quantum Circuit (PQC) structure for U_3 encoding.

- [2] Schuld, M., Sinayskiy, I., Petruccione, F.: An introduction to quantum machine learning. Contemporary Physics **56**(2), 172–185 (2015)
- [3] Ciliberto, C., Herbster, M., Ialongo, A.D., Pontil, M., Rocchetto, A., Severini, S., Wossnig, L.: Quantum machine learning: a classical perspective. Proceedings of the Royal Society A: Mathematical, Physical and Engineering Sciences **474**(2209), 20170551 (2018)
- [4] Lloyd, S., Mohseni, M., Rebentrost, P.: Quantum algorithms for supervised and unsupervised machine learning. arXiv preprint arXiv:1307.0411 (2013)
- [5] Harrow, A.W., Montanaro, A.: Quantum computational supremacy. Nature

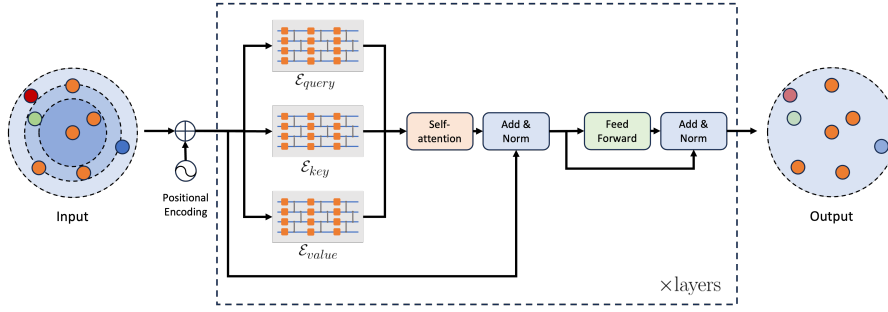


Fig. 8: The framework of Quantum Clusformer $\mathcal{N}(\Phi)$. The input is a cluster, the orange dot points are the samples having the same labels as the centroid while the different colors, i.e., red, blue, and green indicate the noisy and hard samples.

549(7671), 203–209 (2017)

- [6] Preskill, J.: Quantum computing in the nisq era and beyond. *Quantum* **2**, 79 (2018)
- [7] Arute, F., Arya, K., Babbush, R., Bacon, D., Bardin, J.C., Barends, R., Biswas, R., Boixo, S., Brandao, F.G., Buell, D.A., *et al.*: Quantum supremacy using a programmable superconducting processor. *Nature* **574**(7779), 505–510 (2019)
- [8] Zhong, H.-S., Wang, H., Deng, Y.-H., Chen, M.-C., Peng, L.-C., Luo, Y.-H., Qin, J., Wu, D., Ding, X., Hu, Y., *et al.*: Quantum computational advantage using photons. *Science* **370**(6523), 1460–1463 (2020)
- [9] Bharti, K., Cervera-Lierta, A., Kyaw, T.H., Haug, T., Alperin-Lea, S., Anand, A., Degroote, M., Heimonen, H., Kottmann, J.S., Menke, T., *et al.*: Noisy intermediate-scale quantum algorithms. *Reviews of Modern Physics* **94**(1), 015004 (2022)
- [10] Cerezo, M., Arrasmith, A., Babbush, R., Benjamin, S.C., Endo, S., Fujii, K., McClean, J.R., Mitarai, K., Yuan, X., Cincio, L., *et al.*: Variational quantum algorithms. *Nature Reviews Physics* **3**(9), 625–644 (2021)
- [11] Schuld, M., Bocharov, A., Svore, K.M., Wiebe, N.: Circuit-centric quantum classifiers. *Physical Review A* **101**(3), 032308 (2020)
- [12] Grant, E., Benedetti, M., Cao, S., Hallam, A., Lockhart, J., Stojevic, V., Green, A.G., Severini, S.: Hierarchical quantum classifiers. *npj Quantum Information* **4**(1), 65 (2018)
- [13] Cong, I., Choi, S., Lukin, M.D.: Quantum convolutional neural networks. *Nature Physics* **15**(12), 1273–1278 (2019)

- [14] Ostaszewski, M., Trenkwalder, L.M., Masarczyk, W., Scerri, E., Dunjko, V.: Reinforcement learning for optimization of variational quantum circuit architectures. *Advances in Neural Information Processing Systems* **34**, 18182–18194 (2021)
- [15] Ostaszewski, M., Grant, E., Benedetti, M.: Structure optimization for parameterized quantum circuits. *Quantum* **5**, 391 (2021)
- [16] Zhang, S.-X., Hsieh, C.-Y., Zhang, S., Yao, H.: Differentiable quantum architecture search. *Quantum Science and Technology* **7**(4), 045023 (2022)
- [17] Du, Y., Huang, T., You, S., Hsieh, M.-H., Tao, D.: Quantum circuit architecture search: error mitigation and trainability enhancement for variational quantum solvers. *arXiv preprint arXiv:2010.10217* (2020)
- [18] Benedetti, M., Lloyd, E., Sack, S., Fiorentini, M.: Parameterized quantum circuits as machine learning models. *Quantum Science and Technology* **4**(4), 043001 (2019)
- [19] O'Malley, D., Vesselinov, V.V., Alexandrov, B.S., Alexandrov, L.B.: Nonnegative/binary matrix factorization with a d-wave quantum annealer. *PloS one* **13**(12), 0206653 (2018)
- [20] Cavallaro, G., Willsch, D., Willsch, M., Michielsen, K., Riedel, M.: Approaching remote sensing image classification with ensembles of support vector machines on the d-wave quantum annealer. In: *IGARSS 2020-2020 IEEE International Geoscience and Remote Sensing Symposium*, pp. 1973–1976 (2020). IEEE
- [21] Li, J., Ghosh, S.: Quantum-soft qubo suppression for accurate object detection. In: *European Conference on Computer Vision*, pp. 158–173 (2020). Springer
- [22] Golyanik, V., Theobalt, C.: A quantum computational approach to correspondence problems on point sets. In: *Proceedings of the IEEE/CVF Conference on Computer Vision and Pattern Recognition*, pp. 9182–9191 (2020)
- [23] Noormandipour, M., Wang, H.: Matching point sets with quantum circuit learning. In: *ICASSP 2022-2022 IEEE International Conference on Acoustics, Speech and Signal Processing (ICASSP)*, pp. 8607–8611 (2022). IEEE
- [24] Benkner, M.S., Löhner, Z., Golyanik, V., Wunderlich, C., Theobalt, C., Moeller, M.: Q-match: Iterative shape matching via quantum annealing. In: *Proceedings of the IEEE/CVF International Conference on Computer Vision*, pp. 7586–7596 (2021)
- [25] Benkner, M.S., Golyanik, V., Theobalt, C., Moeller, M.: Adiabatic quantum graph matching with permutation matrix constraints. In: *2020 International Conference on 3D Vision (3DV)*, pp. 583–592 (2020). IEEE

- [26] Birdal, T., Golyanik, V., Theobalt, C., Guibas, L.J.: Quantum permutation synchronization. In: Proceedings of the IEEE/CVF Conference on Computer Vision and Pattern Recognition, pp. 13122–13133 (2021)
- [27] Nguyen, X.B., Thompson, B., Churchill, H., Luu, K., Khan, S.U.: Quantum vision clustering. arXiv preprint arXiv:2309.09907 (2023)
- [28] Arrigoni, F., Menapace, W., Benkner, M.S., Ricci, E., Golyanik, V.: Quantum motion segmentation. In: European Conference on Computer Vision, pp. 506–523 (2022). Springer
- [29] Dendukuri, A., Luu, K.: Image processing in quantum computers. arXiv preprint arXiv:1812.11042 (2018)
- [30] Date, P., Schuman, C., Patton, R., Potok, T.: A classical-quantum hybrid approach for unsupervised probabilistic machine learning. In: Advances in Information and Communication: Proceedings of the 2019 Future of Information and Communication Conference (FICC), Volume 2, pp. 98–117 (2020). Springer
- [31] Barkoutsos, P.K., Nannicini, G., Robert, A., Tavernelli, I., Woerner, S.: Improving variational quantum optimization using cvar. *Quantum* **4**, 256 (2020)
- [32] Romero, J., Aspuru-Guzik, A.: Variational quantum generators: Generative adversarial quantum machine learning for continuous distributions. *Advanced Quantum Technologies* **4**(1), 2000003 (2021)
- [33] Liu, J., Lim, K.H., Wood, K.L., Huang, W., Guo, C., Huang, H.-L.: Hybrid quantum-classical convolutional neural networks. *Science China Physics, Mechanics & Astronomy* **64**(9), 290311 (2021)
- [34] Nielsen, M.A., Chuang, I.L.: Quantum computation and quantum information. *Phys. Today* **54**(2), 60 (2001)
- [35] Nguyen, X.-B., Bui, D.T., Duong, C.N., Bui, T.D., Luu, K.: Clusformer: A transformer based clustering approach to unsupervised large-scale face and visual landmark recognition. In: Proceedings of the IEEE/CVF Conference on Computer Vision and Pattern Recognition, pp. 10847–10856 (2021)
- [36] Deng, J., Guo, J., Xue, N., Zafeiriou, S.: Arcface: Additive angular margin loss for deep face recognition. In: Proceedings of the IEEE/CVF Conference on Computer Vision and Pattern Recognition, pp. 4690–4699 (2019)
- [37] Wang, H., Wang, Y., Zhou, Z., Ji, X., Gong, D., Zhou, J., Li, Z., Liu, W.: Cosface: Large margin cosine loss for deep face recognition. In: Proceedings of the IEEE Conference on Computer Vision and Pattern Recognition, pp. 5265–5274 (2018)

- [38] He, K., Zhang, X., Ren, S., Sun, J.: Deep residual learning for image recognition. In: Proceedings of the IEEE Conference on Computer Vision and Pattern Recognition, pp. 770–778 (2016)
- [39] Guo, Y., Zhang, L., Hu, Y., He, X., Gao, J.: Ms-celeb-1m: A dataset and benchmark for large-scale face recognition. In: Computer Vision–ECCV 2016: 14th European Conference, Amsterdam, The Netherlands, October 11–14, 2016, Proceedings, Part III 14, pp. 87–102 (2016). Springer
- [40] Deng, J., Dong, W., Socher, R., Li, L.-J., Li, K., Fei-Fei, L.: Imagenet: A large-scale hierarchical image database. In: 2009 IEEE Conference on Computer Vision and Pattern Recognition, pp. 248–255 (2009). Ieee
- [41] Liu, Z., Mao, H., Wu, C.-Y., Feichtenhofer, C., Darrell, T., Xie, S.: A convnet for the 2020s. In: Proceedings of the IEEE/CVF Conference on Computer Vision and Pattern Recognition, pp. 11976–11986 (2022)
- [42] Yang, L., Zhan, X., Chen, D., Yan, J., Loy, C.C., Lin, D.: Learning to cluster faces on an affinity graph. In: Proceedings of the IEEE/CVF Conference on Computer Vision and Pattern Recognition, pp. 2298–2306 (2019)
- [43] Yang, L., Chen, D., Zhan, X., Zhao, R., Loy, C.C., Lin, D.: Learning to cluster faces via confidence and connectivity estimation. In: Proceedings of the IEEE/CVF Conference on Computer Vision and Pattern Recognition, pp. 13369–13378 (2020)
- [44] Shen, S., Li, W., Wang, X., Zhang, D., Jin, Z., Zhou, J., Lu, J.: Clip-cluster: Clip-guided attribute hallucination for face clustering. In: Proceedings of the IEEE/CVF International Conference on Computer Vision, pp. 20786–20795 (2023)
- [45] Shin, J., Lee, H.-J., Kim, H., Baek, J.-H., Kim, D., Koh, Y.J.: Local connectivity-based density estimation for face clustering. In: Proceedings of the IEEE/CVF Conference on Computer Vision and Pattern Recognition, pp. 13621–13629 (2023)
- [46] Shen, S., Li, W., Zhu, Z., Huang, G., Du, D., Lu, J., Zhou, J.: Structure-aware face clustering on a large-scale graph with 107 nodes. In: Proceedings of the IEEE/CVF Conference on Computer Vision and Pattern Recognition, pp. 9085–9094 (2021)
- [47] Wang, Y., Zhang, Y., Zhang, F., Lin, M., Zhang, Y., Wang, S., Sun, X.: Ada-nets: Face clustering via adaptive neighbour discovery in the structure space. arXiv preprint arXiv:2202.03800 (2022)
- [48] Nguyen, X.-B., Duong, C.N., Savvides, M., Roy, K., Churchill, H., Luu, K.: Fairness in visual clustering: A novel transformer clustering approach. arXiv preprint

arXiv:2304.07408 (2023)

- [49] Ester, M., Kriegel, H.-P., Sander, J., Xu, X., *et al.*: A density-based algorithm for discovering clusters in large spatial databases with noise. In: Kdd, vol. 96, pp. 226–231 (1996)
- [50] Otto, C., Wang, D., Jain, A.K.: Clustering millions of faces by identity. *IEEE transactions on pattern analysis and machine intelligence* **40**(2), 289–303 (2017)
- [51] Wang, Z., Zheng, L., Li, Y., Wang, S.: Linkage based face clustering via graph convolution network. In: *Proceedings of the IEEE/CVF Conference on Computer Vision and Pattern Recognition*, pp. 1117–1125 (2019)
- [52] Li, J., Li, D., Xiong, C., Hoi, S.: Blip: Bootstrapping language-image pre-training for unified vision-language understanding and generation. In: *International Conference on Machine Learning*, pp. 12888–12900 (2022). PMLR
- [53] Yu, J., Wang, Z., Vasudevan, V., Yeung, L., Seyedhosseini, M., Wu, Y.: Coca: Contrastive captioners are image-text foundation models. *arXiv preprint arXiv:2205.01917* (2022)
- [54] Zhai, X., Mustafa, B., Kolesnikov, A., Beyler, L.: Sigmoid loss for language image pre-training. *arXiv preprint arXiv:2303.15343* (2023)
- [55] Luo, Z., Zhao, P., Xu, C., Geng, X., Shen, T., Tao, C., Ma, J., Lin, Q., Jiang, D.: Lexlip: Lexicon-bottlenecked language-image pre-training for large-scale image-text sparse retrieval. In: *Proceedings of the IEEE/CVF International Conference on Computer Vision*, pp. 11206–11217 (2023)
- [56] Wang, T., Lin, K., Li, L., Lin, C.-C., Yang, Z., Zhang, H., Liu, Z., Wang, L.: Equivariant similarity for vision-language foundation models. *arXiv preprint arXiv:2303.14465* (2023)
- [57] Nguyen, X.-B., Duong, C.N., Li, X., Gauch, S., Seo, H.-S., Luu, K.: Micron-bert: Bert-based facial micro-expression recognition. In: *Proceedings of the IEEE/CVF Conference on Computer Vision and Pattern Recognition*, pp. 1482–1492 (2023)
- [58] Nguyen, H.-Q., Truong, T.-D., Nguyen, X.B., Dowling, A., Li, X., Luu, K.: Insect-foundation: A foundation model and large-scale 1m dataset for visual insect understanding. *arXiv preprint arXiv:2311.15206* (2023)
- [59] Nguyen, X.-B., Lee, G.S., Kim, S.H., Yang, H.J.: Self-supervised learning based on spatial awareness for medical image analysis. *IEEE Access* **8**, 162973–162981 (2020)
- [60] Nguyen, X.-B., Lee, G.-S., Kim, S.-H., Yang, H.-J.: Audio-video based emotion recognition using minimum cost flow algorithm. In: *2019 IEEE/CVF International*

- Conference on Computer Vision Workshop (ICCVW), pp. 3737–3741 (2019). IEEE
- [61] Nguyen-Xuan, B., Lee, G.-S.: Sketch recognition using lstm with attention mechanism and minimum cost flow algorithm. *International Journal of Contents* **15**(4), 8–15 (2019)
- [62] Nguyen, X.B., Bisht, A., Churchill, H., Luu, K.: Two-dimensional quantum material identification via self-attention and soft-labeling in deep learning. arXiv preprint arXiv:2205.15948 (2022)
- [63] Nguyen, X.-B., Liu, X., Li, X., Luu, K.: The algonauts project 2023 challenge: Uark-ualbany team solution. arXiv preprint arXiv:2308.00262 (2023)
- [64] Nguyen, X.-B., Li, X., Khan, S.U., Luu, K.: Brainformer: Modeling mri brain functions to machine vision. arXiv preprint arXiv:2312.00236 (2023)
- [65] Serna-Aguilera, M., Nguyen, X.B., Singh, A., Rockers, L., Park, S.-W., Neely, L., Seo, H.-S., Luu, K.: Video-based autism detection with deep learning. In: 2024 IEEE Green Technologies Conference (GreenTech), pp. 159–161 (2024). IEEE
- [66] Chen, S.Y.-C., Yoo, S., Fang, Y.-L.L.: Quantum long short-term memory. In: ICASSP 2022-2022 IEEE International Conference on Acoustics, Speech and Signal Processing (ICASSP), pp. 8622–8626 (2022). IEEE
- [67] Vaswani, A., Shazeer, N., Parmar, N., Uszkoreit, J., Jones, L., Gomez, A.N., Kaiser, L., Polosukhin, I.: Attention is all you need. *Advances in neural information processing systems* **30** (2017)
- [68] Wang, H., Ding, Y., Gu, J., Li, Z., Lin, Y., Pan, D.Z., Chong, F.T., Han, S.: Quantumnas: Noise-adaptive search for robust quantum circuits. In: The 28th IEEE International Symposium on High-Performance Computer Architecture (HPCA-28) (2022)
- [69] Loshchilov, I., Hutter, F.: Sgdr: Stochastic gradient descent with warm restarts. arXiv preprint arXiv:1608.03983 (2016)
- [70] Loshchilov, I., Hutter, F.: Decoupled weight decay regularization. arXiv preprint arXiv:1711.05101 (2017)
- [71] Weyand, T., Araujo, A., Cao, B., Sim, J.: Google Landmarks Dataset v2 - A Large-Scale Benchmark for Instance-Level Recognition and Retrieval. In: Proc. CVPR (2020)
- [72] Lloyd, S.: Least squares quantization in pcm. *IEEE transactions on information theory* **28**(2), 129–137 (1982)

- [73] Sculley, D.: Web-scale k-means clustering. In: Proceedings of the 19th International Conference on World Wide Web, pp. 1177–1178 (2010)
- [74] Sibson, R.: Slink: an optimally efficient algorithm for the single-link cluster method. *The computer journal* **16**(1), 30–34 (1973)
- [75] Zhan, X., Liu, Z., Yan, J., Lin, D., Loy, C.C.: Consensus-driven propagation in massive unlabeled data for face recognition. In: Proceedings of the European Conference on Computer Vision (ECCV), pp. 568–583 (2018)
- [76] Liu, J., Qiu, D., Yan, P., Wei, X.: Learn to cluster faces via pairwise classification. In: Proceedings of the IEEE/CVF International Conference on Computer Vision, pp. 3845–3853 (2021)
- [77] Ho, J., Yang, M.-H., Lim, J., Lee, K.-C., Kriegman, D.: Clustering appearances of objects under varying illumination conditions. In: 2003 IEEE Computer Society Conference on Computer Vision and Pattern Recognition, 2003. Proceedings., vol. 1, p. (2003). IEEE